Dalton Transactions

PAPER

View Article Online
View Journal | View Issue

Cite this: *Dalton Trans.*, 2016, **45**, 18494

Phase pure α-Mn_2O_3 prisms and their bifunctional electrocatalytic activity in oxygen evolution and reduction reactions†

Maryam Jahan,[a,b] Satoshi Tominaka[a,b] and Joel Henzie*[a,b]

Received 9th August 2016,
Accepted 16th September 2016

DOI: 10.1039/c6dt03158g

www.rsc.org/dalton

Synthesizing manganese oxide materials with exact control of the nanoparticle shape and phase is difficult, making it challenging to understand the influence of the surface structure on electrocatalysis. Here we describe an inexpensive, low-temperature method to synthesize single-crystal orthorhombic phase α-Mn_2O_3 prisms bound by the {100} facets. The synthesis is the first method to use the cation bridging effect to assist in the creation of α-Mn_2O_3 prisms. According to structural analysis using X-ray diffraction, X-ray pair-distribution function (PDF) measurements and high resolution transmission electron microscopy, the material is composed exclusively of α-Mn_2O_3 prisms, and no additional amorphous or nanocrystalline phases are present. Heating the prisms transformed the material to a more symmetrical, cubic phase α-Mn_2O_3 that exhibited strong bifunctional electrocatalytic activity for the oxygen evolution (OER) and oxygen reduction (ORR) reactions. We compared the oxygen electrode activities (OEA) and found that the α-Mn_2O_3 prisms performed 79% better than commercially-produced α-Mn_2O_3 powders, indicating that these α-Mn_2O_3 prisms perform well as inexpensive, earth-abundant materials for reversible electrodes.

Introduction

Preparing nanomaterials having well-organized surface structures has been a rich area of research because the selectivity and reactivity of heterogeneous catalysts depend on exposed crystallographic surfaces. This is particularly evident in the field of noble metal catalysis, where successive advances in the way we synthesize colloids have led to extraordinary enhancements in mass activity and specific activity.[1,2] This level of success in utilizing noble metals is encouraging researchers to pursue new, more earth abundant material targets,[3] extending this level of control to create materials with high activities that also possess the lowest economic and environmental cost.[4] Additionally, good control of particle shape should enable the assembly of large-scale ordered functional materials that can be completely assembled from the bottom up.[5–7]

Manganese oxide is an interesting target for colloidal chemistry because $CaMn_4O_5$ clusters form the inorganic core of the water oxidizing complex in photosystem II.[8] Taking this inspiration from nature, researchers have created solid-state equivalents based on manganese oxide polymorphs to test how catalysis is affected by changes in the structure.[9,10] Electrodeposited nanostructured manganese oxide (MnO_x) films can behave as bifunctional catalysts for the oxygen evolution (OER) and oxygen reduction reactions (ORR).[11,12] However, determining the surface structure of this material is not trivial, because polycrystalline films are not necessarily phase-pure and contain multiple crystal facets. As a result, the electrochemical properties of MnO_x films are highly dependent on the crystalline structure of the catalyst. We strongly believe that pure materials with precise control of phase and shape are needed to truly understand the catalytic behaviour of manganese oxide materials in their various forms. Here we report a simple, low-temperature method to synthesize phase-pure α-Mn_2O_3 prisms bound by the {100} facets (Fig. 1). The as-synthesized prisms adopt the orthorhombic bixbyite phase, and can be transformed to the cubic phase by thermal treatment. We hypothesize that the surface structure and phase purity will impact their activity in oxygen electrochemistry.

[a]*International Center for Materials Nanoarchitectonics (WPI-MANA), 1-1 Namiki, Tsukuba, Ibaraki 305-0044, Japan*
[b]*National Institute for Materials Science (NIMS), 1-1 Namiki, Tsukuba, Ibaraki 305-0044, Japan. E-mail: HENZIE.Joeladam@nims.go.jp*
†Electronic supplementary information (ESI) available. See DOI: 10.1039/c6dt03158g

Experimental

Preparation of orthorhombic and cubic phase α-Mn_2O_3 prisms

Colloidal α-Mn_2O_3 prisms bound by the {100} facets were synthesized using a low-temperature hydrothermal method. 8.7 mg of $LiMn_2O_4$ powder and 35 mg of NaAOT were dis-

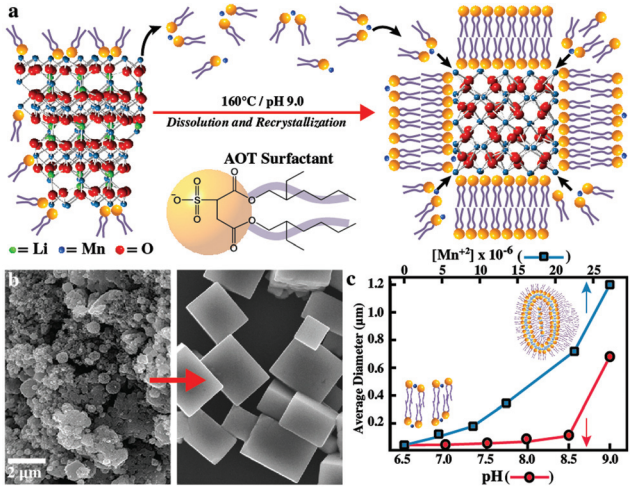

Fig. 1 (a) Scheme describing the low-temperature hydrothermal synthesis of α-Mn_2O_3 prisms from $LiMn_2O_4$ powder. AOT surfactant assists in the dissolution and recrystallization of the prisms. (b) SEM micrographs showing the $LiMn_2O_4$ powder precursor (left) and α-Mn_2O_3 product (right). The scale bar applies to both SEM images and (c) dynamic light scattering (DLS) measurements of a 5 mM aqueous NaAOT (2× CMC) solution titrated with NaOH (red curve) or Mn(II) acetate (blue curve). High pH and high Mn^{2+} both trigger the formation of lamellar and spherulitic assemblies that can serve as templates for the formation of nanoparticles.

persed in 15 mL of water using sonication. After mixing, the pH of the reagent solution was adjusted to 9.0 and then heated in a stainless-steel autoclave for 48 hours at 160 °C. The samples were then allowed to slowly cool to room temperature over several hours. The Teflon liner was opened to reveal a black liquid containing the α-Mn_2O_3 prisms.

General instrumentation

Scanning electron microscopy (SEM) micrographs were recorded on an S-4800 Hitachi field emission SEM. High resolution transmission electron microscopy (HRTEM) measurements were performed at 200 keV with a JEOL 2000 EX. The HRTEM images were modelled using QSTEM software. Dynamic light scattering (DLS) measurements were collected on a Delsa Nano C Particle analyser (Beckman Coulter). X-ray photoelectron spectroscopy (XPS) measurements were acquired on a high resolution XPS system with a monochromated Al K-alpha source using charge compensation (Thermo-Fisher Theta Probe). Powder X-ray diffraction (PXRD) measurements were carried out using a Rigaku RINT 2000 ULTIMA 3 with CuKα radiation (λ = 1.54060 Å) with the incident beam calibrated by SiO_2. The powder patterns were analysed by a Pawley fitting with GSASII software[13] and simulated using Mercury.[14]

Pair distribution function analysis

X-ray total scattering data were collected on a Rigaku Rapid-S diffractometer at room temperature (27 °C) using a Ag K_α (λ = 0.560883 Å) source operated at 50 kV (40 mA). Both the synthesized and heated prisms were placed in a dry N_2 glove box and then transferred to Lindemann glass capillaries with an inner diameter of 1 mm (Hilgenberg). The capillaries were temporarily sealed with a parafilm, moved outside the glovebox and then sealed with an open flame. The scattering data were collected on a curved imaging plate for 20 min, and more than 40 measurements were integrated to obtain sufficient intensities at the magnitude of the scattering vector, Q, of 22 $Å^{-1}$. Background subtraction, X-ray polarization correction, absorption correction, energy dependence of scattering factors, and Compton scattering correction were performed using the PDFgetX2 program.[15] The structure functions, $S(Q)$, were further treated to remove the slowly changing oscillation which is not associated with the structure of the materials. The goniometer or wavelength was calibrated using a NIST standard CeO_2 (674B, a = 5.411651(6), phase purity 91%), and the $K\alpha_2$ radiation was removed using the Rachinger correction ($K\alpha_1$, λ = 0.55978 Å).[16] Finally, the structure functions (Q_{max} = 22.0 $Å^{-1}$) were converted into PDFs through the discrete sine transform:

$$G(r) = 4\pi\rho_0 r(g(r) - 1) = \frac{2}{\pi}\int_{Q_{min}}^{Q_{max}} Q(S(Q) - 1)\sin(Qr)\mathrm{d}Q$$

where $G(r)$ is the reduced pair distribution function, and $g(r)$ is the pair-distribution function.[17] The structure of the material was analysed by the real-space Rietveld analysis using PDFgui software[18] in the PDF range of 0–40 Å.

Electrochemical measurements

To prepare the α-Mn_2O_3 prisms for electrochemical measurements, 5 milligrams of the synthesized sample was mixed with the following solution: 2 mL ethanol, 3 mL ultrapure water, and 50 μL Nafion (5 wt%). This solution was sonicated for 30 minutes to achieve homogeneous ink. Then a 5 μL drop of the catalyst ink was loaded on the polished surface of the interchangeable GC disk and dried slowly at room temperature to achieve a uniform surface. Once the sample was completely dried we weighed it on an analytical balance to estimate the mass of α-Mn_2O_3 prisms delivered to the surface. Over four trials the weight was 5 ± 0.21 μg (*i.e.* 40 ± 0.21 μg cm^{-2}) and had uniform coverage according to SEM (ESI Fig. S1†). To prepare the electro-active cubic phase α-Mn_2O_3 prisms, the interchangeable GC electrode was heated to 480 °C in air for 10 hours. The orthorhombic phase sample was applied to the GC electrode in the same way, but the 480 °C heating step was omitted. We compared the catalytic activity of the prisms with commercially produced α-Mn_2O_3 powder (Sigma Aldrich). The commercial powder was deposited on the GCE and processed in the same way as the α-Mn_2O_3 prisms (see Experimental Section). Since the 480 °C heating step might affect the GC electrode, we examined the LSV curves of the bare GC before and after heat treatment at 480 °C (ESI Fig. S2†). There was very little change, indicating that oxidative damage was negligible. Finally, a 20 wt% Pt/C catalyst was used as comparison and prepared exactly as the synthesized prisms to achieve a similar loading of 5 ± 0.25 μg of 20 wt% Pt/C (*i.e.* 40 ± 0.25 μg cm^{-2}). The Pt/C sample was measured immediately after drying at room temperature.

All measurements were carried out at room temperature using a potentiostat (Biologic VMP3) with a three-electrode electrochemical cell. Rotating disk electrode (RDE) and rotating ring disk electrode (RRDE) measurements were performed on an RRDE-3A (ALS Co., Ltd) system. We used an interchangeable glassy carbon (GC) disk electrode with a 4 mm diameter (area ~0.125 cm^2) as the working electrode, a platinum (Pt) wire as the counter electrode, and Hg/HgO (1 M NaOH) as the reference electrode. The potential of the reference electrode (Hg/HgO, 1 M NaOH) in 0.1 M KOH shifts to 0.870 V *vs.* The reversible hydrogen electrode (RHE) based on our calculations, which is in agreement with the value reported in the literature.[11] For the RRDE measurements we used a Pt ring (2 mm)/GC disk (4 mm) electrode. The GC disk was mechanically polished to achieve a mirror-like finish on the top surface of the electrode. Finally the GC electrode was sonicated in ultrapure water, ethanol, and then again in ultrapure water and dried at room temperature before applying the catalyst ink.

Linear sweep voltammetry (LSV) measurements were performed in O_2-saturated 0.1 M KOH solutions at a scan rate of 10 mV s^{-1}. LSVs were measured using forward and backward currents to confirm the reversibility of the catalysts (ESI Fig. S3†). Further stability experiments were conducted by cycling α-Mn_2O_3 prisms 300-times (ESI Fig. S4†). The cycled particles under OER (0.87 V to 2.07 V *vs.* RHE) or ORR (0.17 V to 0.87 V *vs.* RHE) were imaged using scanning TEM (STEM) in annular dark field mode. The STEM images show that the particles begin to roughen under both conditions, but that the overall shape of the particles remains unchanged and that reactions occur near the surface (ESI Fig. S5†). HRTEM measurements taken from the edge of the OER-exposed prisms match well the {200} lattice spacing of MnO_x-like birnessite. For the samples cycled under ORR conditions we observed 0.288 nm spacings characteristic of the {200} plane of Mn_3O_4 (ESI Fig. S5†). The CV experiments were conducted in O_2 and N_2-saturated 0.1 M KOH solution typically at a scan rate of 50 mV s^{-1}. In N_2-saturated 0.1 M KOH at 50 mV s^{-1}, we observed an oxidation feature at 0.89 V which is associated with the oxidation of $Mn^{III}_2O_3$ to $Mn^{IV}O_2$, whereas the cathodic current peak at 0.67 V is the reverse reaction corresponding to reduction of $Mn^{III}_2O_3$ to $Mn^{II,III}_3O_4$ (ESI Fig. S6†).[19] The comparison of CV of the GC electrode and α-Mn_2O_3 proves the improvement of the conductivity of this sample (ESI Fig. S6†). RDE measurements were performed at rotation rates varying from 500 to 3000 rpm depending on the measurement, with the scan rate of 10 mV s^{-1}. RDDE measurements were carried out at 2000 rpm rotation rate with the scan rate of 10 mV s^{-1}.

Results and discussion

Using dissolution and "cation-bridging" to form α-Mn_2O_3 prisms

The scheme in Fig. 1a describes the colloidal reaction mechanism. $LiMn_2O_4$ powder is completely dispersed in an aqueous solution of the NaAOT surfactant (pH = 9.0) under hydrothermal conditions, and then recrystallized into α-Mn_2O_3 prisms bound by sharp, rectangular facets (Fig. 1b). We regard a high concentration of oxygen as important to achieve control over the shape and phase in the colloidal reaction. Reagent solutions that were sparged with N_2 gas prior to the hydrothermal reaction did not form prisms, whereas solutions sparged with pure O_2 formed nicely facetted prisms. This is not surprising because it is known from gas phase synthesis methods that a high oxygen partial pressure is necessary to achieve the α-Mn_2O_3 phase.[20]

In the reaction $LiMn_2O_4$ powder is used as the starting material because it is inexpensive and can contribute excess oxygen inside the reaction vessel as the spinel framework is dissolved:

$$2LiMn_2O_4 \rightarrow 2Li^+ + 2\alpha\text{-}Mn_2O_3 + 1O_2$$

The dissolution of $LiMn_2O_4$ is well studied due to the phenomenon of capacity fading in Li-ion batteries.[21] $LiMn_2O_4$ can dissolve according to the disproportionation reaction.[22] This results in either the complete dissolution of the spinel framework, or partial dissolution of Mn and retention of some of the oxide lattice. Partial dissolution of the Mn-oxide lattice in solution could lead to a seed-mediated growth mechanism. For example, Zhang *et al.* used bulky commercial $LiMn_2O_4$ powders (average size ~5 μm) in aqueous NaAOT solution to grow $LiMn_2O_4$ nanobelts.[23] We found that smaller sized $LiMn_2O_4$ powders (average size <500 nm) also formed nanobelts and wires under basic conditions, but these 1-D structures eventually dissolved to form α-Mn_2O_3 prisms (ESI Fig. S7†). Thus the smaller size of the powder was very important in determining the phase and morphology because complete dissolution is necessary to obtain the α-Mn_2O_3 prisms. Under the same reaction conditions bulky $LiMn_2O_4$ powders (average size <5 μm) eventually form γ-MnOOH rods (ESI Fig. S8†).

A surfactant often plays a central role in controlling the morphology and phase of nanomaterials in colloidal reactions.[24] The sodium AOT surfactant is typically used in reverse micelle-based synthetic schemes, but its interaction with oxide surfaces in water is quite intriguing. In our synthesis, the anionic AOT surfactant appears to preferentially etch manganese oxide materials containing Mn^{4+} cations. This was not only the case for $LiMn_2O_4$, commercially purchased α-Mn_2O_3 (Sigma Aldrich, 99.99%) also contains a noticeable impurity of Mn^{4+}-containing MnO_2 according to PXRD analysis (ESI Fig. S9†). After hydrothermal treatment with AOT using the synthesis conditions, the MnO_2 impurity in the commercial Mn_2O_3 sample was etched away. These data show that Mn_2O_3 is the most stable phase in the presence of AOT, and that Mn oxides containing some fraction of Mn^{4+} cations such as $LiMn_2O_4$ and MnO_2 are not stable. Incidentally, hydrothermal treatment in AOT might be a cheap method to prepare clean Mn^{3+} surfaces.

Other researchers have discovered that AOT has a high affinity for charged surfaces—even like-charged surfaces—in

the presence of divalent cations.[25] This enhanced absorption has been attributed to "cation-bridging", where two AOT molecules become associated with each divalent cation, typically in aqueous solutions at high pH. AOT adsorbs onto the surface, creating a lamellar phase that can assist in the dissolution of minerals by cation exchange.[26] Fig. 1c shows dynamic light scattering (DLS) measurements of a 5 mM aqueous solution (2× the critical micelle concentration or CMC) of NaAOT titrated with NaOH or Mn(II) acetate. Starting at neutral pH the relative size of AOT aggregates increases as the solution becomes more basic, ultimately forming larger spherulitic and multi-lamellar structures. We also observed a similar trend with the addition of Mn acetate. Like other divalent cations, Mn^{2+} can bridge AOT molecules to stabilize supramolecular structures.

We propose that high pH assists in the adsorption of lamellar-phase NaAOT onto the surface of $LiMn_2O_4$. NaAOT converts to $Mn(AOT)_2$ at the surface and eventually desorbs and moves into the solution, forming micelles and lamellar networks. Reactions performed without the NaAOT surfactant yielded $LiMn_2O_4$ nanowires (ESI Fig. S10†). Reactions performed at low pH resulted in λ-MnO_2.[27] The AOT surfactant was essential for complete dissolution of the starting material by driving the chemical equilibrium toward disproportionation. AOT also assists in the recrystallization of the prisms, and since its adhesion is dependent on high pH, it can be easily washed away with neutral pH water. To our knowledge this is the first report describing the use of the cation bridging effect to assist in the synthesis of a nanoparticle.

Structural analysis of α-Mn_2O_3 prisms: proof of phase purity and phase transformation

After synthesis, the prisms were washed several times in neutral water to remove the AOT surfactant. HRTEM was used to characterize the shape and crystallographic orientation of the prisms (Fig. 2a–d). Electron diffraction performed on several prisms all matched the expected pattern for α-Mn_2O_3 oriented along the <100> axis (Fig. 2b). HRTEM micrographs taken near the centre of the prism have the {200} planes that show the characteristic 0.470 nm lattice spacing (Fig. 2c). The {200} planes are parallel to the surface of the prism observed along the [100] axis, thus the prisms are bound exclusively by the {100} planes. At the edge of the prism, it is possible to resolve the {222} planes, which extend all the way to the edge of the crystal (Fig. 2d). The TEM image of α-Mn_2O_3 observed along the [100] axis was simulated and superimposed on the experimental image (Fig. 2d, inset) and matches the spacings of the (200) and (222) crystal planes.

The orthorhombic phase of α-Mn_2O_3 is known to be the most stable at room temperature with a distorted bixbyite-type structure (a = 9.4157(3), b = 9.4233(3) and c = 9.4047(3) Å) in the *Pcab* space group. However, the material is known to transform to the cubic phase (a = ~9.415 Å) in the *Ia*3 space group at ~302 K.[28] We hypothesize that near the phase transition there should exist a range of metastable structures with varying degrees of distortion between the perfect cubic and the orthorhombic phase of α-Mn_2O_3. The similarity in the crystal structure, and the near room temperature phase transformation, has made it difficult to define the precise phase of α-Mn_2O_3 and whether it is orthorhombic or more cube-like. The PXRD pattern of the freshly synthesized prisms was analysed with a Pawley fitting, but the goodness-of-fit parameters of the simulated orthorhombic structure (1.59) and the cubic structure (1.45) were not definitive enough to conclusively identify the structure (Fig. 3a). But by checking the simulated pattern (Fig. 3a, top) and comparing the reflection lists of the orthorhombic phase and the cubic phase, we found that the prisms had a tiny peak at 28.4°, that is not assignable to the precursors. Thus the synthesized material is likely the orthorhombic phase. These samples were heated at 480 °C for 10 hours and then cooled to room temperature (24–25 °C) and then their powder PXRD pattern was collected. The peak at 28.4° disappeared, indicating that a phase transition from the orthorhombic to the cubic structure (ESI Fig. S11†) occurred, and this was stable even at room temperature. Additionally, the particles still maintain their shape as confirmed by SEM (ESI Fig. S12†).

This proposed phase transition was further studied using pair distribution function (PDF) analysis (Fig. 3b). PDF is a

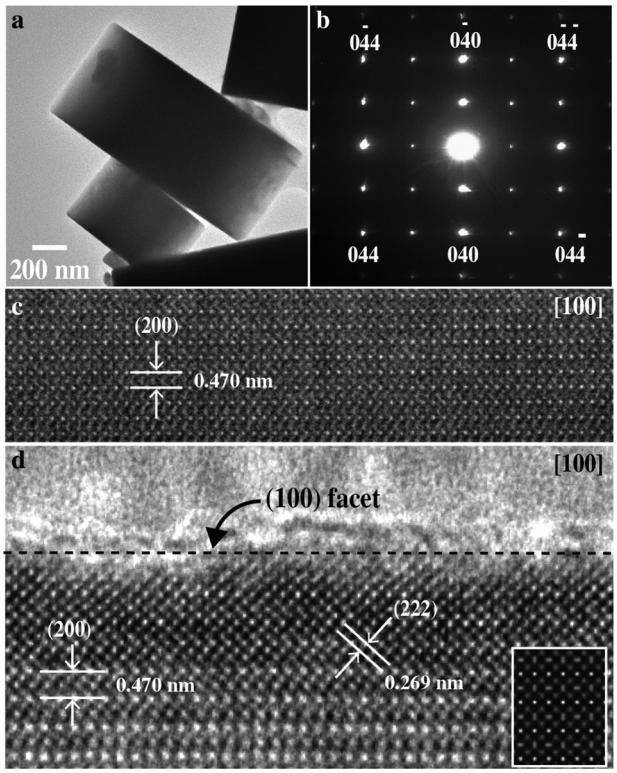

Fig. 2 (a, b) TEM micrograph of an α-Mn_2O_3 prism and the corresponding selected area electron diffraction pattern along the [100] axis. HRTEM micrograph taken from the centre of the α-Mn_2O_3 prism matches the lattice spacing of the (200) planes (c). At the edge of the prism, it is possible to resolve the (222) planes of α-Mn_2O_3 (d). Inset shows the simulated HRTEM image of the crystal along the [100] axis, which matches both lattice spacings for α-Mn_2O_3.

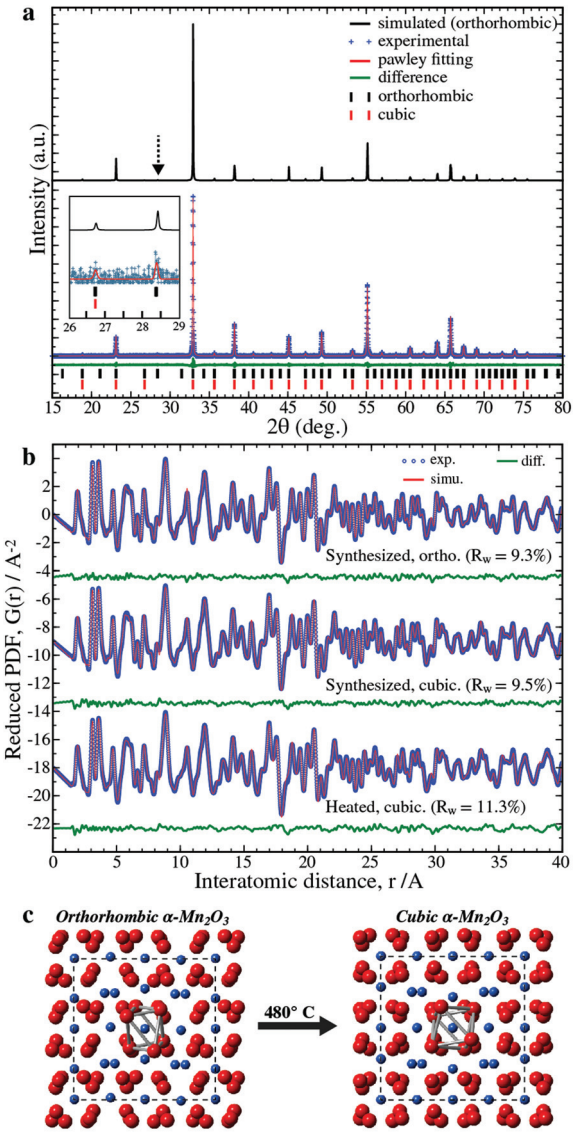

Fig. 3 A structural analysis of the α-Mn_2O_3 prisms. (a) PXRD patterns of the newly synthesized prisms (blue dots) analysed by a Pawley fitting (red curve), compared with a simulated pattern based on the orthorhombic α-Mn_2O_3 structure. The calculated Bragg peak positions for the orthorhombic phase and the cubic phase are shown at the bottom. (b) X-ray pair distribution functions (PDFs) of the prisms analysed by the real-space Rietveld method: top, synthesized product fitted with the orthorhombic α-Mn_2O_3; middle, synthesized product fitted with the cubic α-Mn_2O_3; bottom, thermally treated prisms fitted with the cubic phase α-Mn_2O_3 structure. (c) Orthorhombic and cubic α-Mn_2O_3 structures derived from PDF show the tiny change in bonding arrangement.

powerful tool to refine the atomic positions in nanomaterials, as well as identify amorphous or nanocrystalline phases which are not detectable by PXRD.[17,29] Our PDF analysis shows that the prisms are composed exclusively of α-Mn_2O_3, ruling out the presence of other materials. Assuming the cubic symmetries for both prisms, the lattice of the newly synthesized prisms apparently contracted (a = 9.4086(13) Å, fitting quality R_w = 9.53%) compared with the thermally treated prisms (9.4149(7) Å, R_w = 11.3%), which is close to the typical value for the cubic phase, 9.415 Å.[28] This discrepancy in the lattice constants suggests that the synthesized prisms are indeed composed mainly of the orthorhombic phase (a = 9.4094(15), b = 9.4172(15) and c = 9.3986(15) Å, R_w = 9.27%; note that the relative values of the constants were fixed to those of the reported values)[28] which supports our PXRD data.

In manganese oxides, electronically degenerate Mn(III) tends to exhibit higher specific activities for the ORR[4] and also are more active for the OER.[30] Mn(III) has orbital configurations that depend sensitively on the symmetry and spacing of the MnO_6 octahedral subunits, which will in turn affect the electronic structure. While there is presently no single "descriptor" for catalytic activity in these systems, the Mn(III) moiety and longer Mn–O bond lengths are thought to contribute to structural flexibility at the active site, and higher catalytic activity.[30] Fig. 3c shows the PDF-obtained crystal structures of the orthorhombic and cubic phase α-Mn_2O_3. The volume of the unit cell increased by ~0.2% from the orthorhombic to the cubic phase. Considering just the center MnO_6 octahedron, it is clear that thermal treatment relieves some of the Jahn–Teller distortion, resulting in a ~4% increase in average bond length at this site. Tiny changes in the bond length and bond angle throughout the entire material should collectively affect how the electronic structure of the α-Mn_2O_3 material interacts with the absorbed oxygen.

The surface of manganese oxides might take on different structures and reconstructions depending on temperature and oxygen partial pressure.[31] High resolution X-ray photoelectron spectroscopy (XPS) was used to determine if there was a change in the oxidation state of manganese at the surface of the prisms upon thermal treatment in air. α-Mn_2O_3 has a characteristic separation of the Mn-2$p_{1/2}$ satellite structure (ΔE-2$p_{1/2}$), as well as splitting of the Mn-3s multiplet (ΔE-3s). The primary detection depth of the XPS measurement is ~2.1 nm for the Mn-2p region and ~3.3 nm for the Mn-3s region (*i.e.* the inelastic mean free paths of α-Mn_2O_3).[32] The splittings for the orthorhombic phase prisms were ΔE-2$p_{1/2}$ = 9.98 eV and ΔE-3s = 5.6 eV, closely matching the reported values for α-Mn_2O_3.[33] These features are retained even in the cubic phase prisms (ΔE-2$p_{1/2}$ = 10.0 eV and ΔE-3s = 5.6 eV), so we concluded that thermal treatment causes no change in the oxidation state of the α-Mn_2O_3 surface and it remained Mn(III) (ESI Fig. S13†).

Examining the oxygen reduction (ORR) and oxygen evolution reactions (OER)

Fig. 4 shows the combined OER–ORR performance of the cubic phase α-Mn_2O_3 prisms compared with commercial α-Mn_2O_3 powder and Pt/C (20 wt%) in alkaline media (0.1 M KOH) using LSV. For ORR, the onset potentials at −0.1 mA cm^{-2} were 0.747 V, 0.590 V and 1.047 V for the α-Mn_2O_3 prisms, commercial α-Mn_2O_3 powder and Pt/C, respectively. A larger Tafel slope indicates that a larger resistance (or a large loss of potential) is necessary to accelerate a chemical reaction. The Tafel slope was the highest for commer-

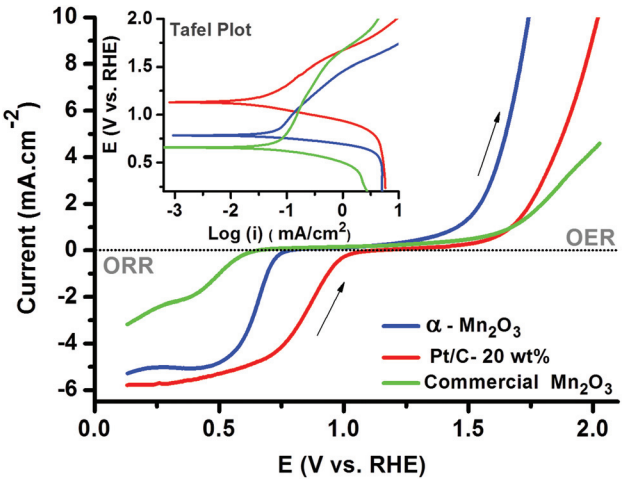

Fig. 4 ORR and OER activities of the cubic phase α-Mn_2O_3 prisms compared to commercial α-Mn_2O_3 powder and Pt/C (Pt-20 wt%) catalyst. Inset, the Tafel plot in OER and ORR regions.

cial α-Mn_2O_3 (169 mV per decade), followed by α-Mn_2O_3 prisms (128 mV per decade) (inset, top left, Fig. 4). 20 wt% Pt/C was the lowest at 121 mV per decade. Generally, on a pure Pt surface the first electron transfer is the rate-determining step resulting in a Tafel slope of 120 mV per decade at high overpotentials.[34] Unsurprisingly, the Pt/C catalyst performed the best, but the α-Mn_2O_3 prisms were close in performance and much better than the commercial α-Mn_2O_3 powder. A more detailed description of ORR activity including the electron transfer number and details on hydrogen peroxide production are included in the ESI Fig. S14–S16.†

For the OER, the onset potentials at 0.1 mA cm^{-2} were 0.956 V for α-Mn_2O_3 prisms, 1.16 V for commercial α-Mn_2O_3 and 1.30 V for 20% Pt/C. The potential at I = 10 mA cm^{-2} for commercial α-Mn_2O_3 is at 2.39 V, which is higher than the α-Mn_2O_3 at 1.74 V. Again we used the Tafel slope to compare the performance of the three catalysts for the OER. The Tafel slope of the α-Mn_2O_3 was 146 mV per decade. By comparison, commercial α-Mn_2O_3 was 231 mV per decade and Pt/C was 122 mV per decade. These measurements show that the performance of an active site on the surface of α-Mn_2O_3 prisms is better than commercial Mn_2O_3.

The combined LSV curves for the α-Mn_2O_3 prisms (both cubic and orthorhombic phase), commercial α-Mn_2O_3 powders, Pt/C-20 wt%, and bare GC are included in ESI Fig. S17.† It is worth noting that the performance of the orthorhombic phase α-Mn_2O_3 prisms was inferior to the cubic phase α-Mn_2O_3 prisms. This could be caused by an inherent difference in the catalytic activity of the two phases, or by the difference in how the electrodes were prepared.

Comparing oxygen electrode activities (OEA)

To understand the influence of the surface structure on catalysis, we compared the oxygen electrode activity (OEA) of the cubic phase α-Mn_2O_3 prisms with other materials including commercial Mn_2O_3 powder. The OEA is the difference between the OER and ORR, and serves as a metric to access how close a material is to the ideal reversible electrode. Here the OEA is calculated using these current densities: ORR at −3 mA cm^{-2} and OER at 10 mA cm^{-2}. Smaller OEA values indicate that performance is closer to the ideal reversible oxygen electrode. The OEA of the cubic phase α-Mn_2O_3 prisms and various materials including precious metals and commercially purchased α-Mn_2O_3 powders are described in Table 1. The OEA of the commercial powder was 1.99 V, or 79% higher than the α-Mn_2O_3 prisms. This high OEA could conceivably be attributed to the presence of the tiny β-MnO_2 impurity (ESI Fig. S9†). Interestingly, when we treated this commercial powder in an aqueous solution of the AOT surfactant at pH = 9 that matched the original synthesis conditions of the prisms, the β-MnO_2 impurity disappeared (ESI Fig. S9†). This observation supports our conclusion that the AOT surfactant is responsible for the phase purity of the prisms because it preferentially etches Mn^{4+} cations. Still, the OEA of this AOT-treated commercial sample dropped only moderately, to 1.73 V, which was ~56% less performance than the OEA of the cubic phase α-Mn_2O_3 prisms. These findings show that phase pure single crystal α-Mn_2O_3 prisms with the {100} facets have high bifunctional activity for oxygen electrochemistry, and that their performance is almost on par with expensive precious metal catalysts.

Table 1 Comparison of OEA activities of α-Mn_2O_3 prisms with commercial α-Mn_2O_3 powder, commercial α-Mn_2O_3 powder treated with AOT, and precious metal catalysts such as Pt/C, Ru/C (from ref. 11) and Ir/C (from ref. 11). OEA is the difference between OER and ORR values. All ORR measurements here correspond to E (V) at I = −3 mA cm^{-2}, while OER is E (V) at I = 10 mA cm^{-2}. An OEA of zero corresponds to an idea reversible oxygen electrode

Material	OER: E (V) at I = 10 mA cm^{-2}	ORR: E (V) at I = −3 mA cm^{-2}	OEA: Δ(OER−ORR)
Cubic α-Mn_2O_3 prism	1.74	0.63	1.11
Commercial α-Mn_2O_3	2.39	0.40	1.99
Commercial α-Mn_2O_3 treated with AOT	2.14	0.41	1.73
Pt/C (20 wt%)	2.01	0.83	1.18
Ir/C (20 wt%)[11]	1.61	0.69	0.92
Ru/C (20 wt%)[11]	1.62	0.61	1.01

Conclusions

The numerous valences of manganese oxide make it an attractive material for catalysis. But in the context of nanomaterial synthesis, creating a phase-pure form of manganese oxide with well-controlled surfaces can be difficult to achieve, and difficult to prove. We have described an inexpensive, low-temperature method to synthesize phase pure α-Mn_2O_3 prisms bound by the {100} facets. This is possible in part because the anionic AOT surfactant preferentially stabilizes the Mn(III) moiety over other oxidation states, which is assisted by the cation bridging effect that was recently observed with AOT.[25] Our synthetic results suggest that this cation bridging effect has the potential as a low-cost, low temperature way to synthesize colloids and activate metal oxide catalysts.

The surface structure has a role in determining catalytic activity. Separating its influence on catalytic enhancement is difficult because researchers are often examining polycrystalline materials with unknown phase purity and bound by surfaces with multiple crystallographic orientations. Our comparison of α-Mn_2O_3 with commercial powder shows that the {100} facet has higher activity than polycrystalline materials. Additionally, we used AOT to clean the surface of the commercial sample and show that the cubic phase α-Mn_2O_3 prisms still possess superior catalytic activities. By combining shape-controlled colloidal synthesis with careful structural characterization and the assistance of theoretical modeling, we hope to elaborate more on the details of the electronic structure in manganese oxides and mixed manganese oxides, and its role in determining catalytic activity.

Acknowledgements

This work was supported by the World Premier International Research Center Initiative on "Materials Nanoarchitectonics (WPI-MANA)" from MEXT, Japan and the Japan Society for the Promotion of Science (JSPS) Bilateral Joint Research Program.

Notes and references

1 L. Zhang, L. T. Roling, X. Wang, M. Vara, M. Chi, J. Liu, S. Choi, J. Park, J. A. Herron, Z. Xie, M. Mavrikakis and Y. Xia, *Science*, 2015, **349**, 412–416.
2 C. Chen, Y. Kang, Z. Huo, Z. Zhu, W. Huang, H. L. Xin, J. D. Snyder, D. Li, J. A. Herron, M. Mavrikakis, M. Chi, K. L. More, Y. Li, N. M. Markovic, G. A. Somorjai, P. Yang and V. R. Stamenkovic, *Science*, 2014, **343**, 1339–1343.
3 H. Hosono, K. Hayashi, T. Kamiya, T. Atou and T. Susaki, *Sci. Technol. Adv. Mater.*, 2011, **12**, 34303.
4 K. A. Stoerzinger, M. Risch, B. Han and Y. Shao-Horn, *ACS Catal.*, 2015, **5**, 6021–6031.
5 S. C. Glotzer and M. J. Solomon, *Nat. Mater.*, 2007, **6**, 557–562.
6 J. Henzie, M. Grünwald, A. Widmer-Cooper, P. L. Geissler and P. Yang, *Nat. Mater.*, 2012, **11**, 131–137.
7 J. Henzie, S. C. Andrews, X. Y. Ling, Z. Li and P. Yang, *Proc. Natl. Acad. Sci. U. S. A.*, 2013, **110**, 6640–6645.
8 Y. Umena, K. Kawakami, J. R. Shen and N. Kamiya, *Nature*, 2011, **473**, 55–60.
9 Y. Meng, W. Song, H. Huang, Z. Ren, S. Y. Chen and S. L. Suib, *J. Am. Chem. Soc.*, 2014, **136**, 11452–11464.
10 U. Maitra, B. S. Naidu, A. Govindaraj and C. N. R. Rao, *Proc. Natl. Acad. Sci. U. S. A.*, 2013, **110**, 11704–11707.
11 Y. Gorlin and T. F. Jaramillo, *J. Am. Chem. Soc.*, 2010, **132**, 13612–13614.
12 Y. Gorlin, B. Lassalle-Kaiser, J. D. Benck, S. Gul, S. M. Webb, V. K. Yachandra, J. Yano and T. F. Jaramillo, *J. Am. Chem. Soc.*, 2013, **135**, 8525–8534.
13 B. H. Toby and R. B. Von Dreele, *J. Appl. Crystallogr.*, 2013, **46**, 544–549.
14 C. F. Macrae, P. R. Edgington, P. Mccabe, E. Pidcock, G. P. Shields, R. Taylor, M. Towler and J. van de Streek, *J. Appl. Crystallogr.*, 2006, **39**, 453–457.
15 X. Qiu, J. W. Thompson and S. J. L. Billinge, *J. Appl. Crystallogr.*, 2004, **37**, 678.
16 W. A. Rachinger, *J. Sci. Instrum.*, 1948, **25**, 254–255.
17 T. Egami and S. J. L. Billinge, *Underneath the Bragg peaks: structural analysis of complex materials*, Elsevier, Oxford, UK, 1st edn, 2003.
18 C. L. Farrow, P. Juhas, J. W. Liu, D. Bryndin, E. S. Božin, J. Bloch, T. Proffen and S. J. L. Billinge, *J. Phys.: Condens. Matter*, 2007, **19**, 335219.
19 H.-Y. Su, Y. Gorlin, I. C. Man, F. Calle-Vallejo, J. K. Nørskov, T. F. Jaramillo and J. Rossmeisl, *Phys. Chem. Chem. Phys.*, 2012, **14**, 14010–14022.
20 H. Xia, Y. Wan, F. Yan and L. Lu, *Mater. Chem. Phys.*, 2014, **143**, 720–727.
21 J. Park, J. H. Seo, G. Plett, W. Lu and A. M. Sastry, *Electrochem. Solid-State Lett.*, 2011, **14**, A14–A18.
22 R. J. Gummow, A. de Kock and M. M. Thackeray, *Solid State Ionics*, 1994, **69**, 59–67.
23 L. Zhang, J. C. Yu, A.-W. Xu, Q. Li, K. W. Kwong and L. Wu, *Chem. Commun.*, 2003, **1**, 2910–2911.
24 M.-P. Pileni, *Nat. Mater.*, 2003, **2**, 145–150.
25 X. Wang, S. Y. Lee, K. Miller, R. Welbourn, I. Stocker, S. Clarke, M. Casford, P. Gutfreund and M. W. A. Skoda, *Langmuir*, 2013, **29**, 5520–5527.
26 I. N. Stocker, K. L. Miller, R. J. L. Welbourn, S. M. Clarke, I. R. Collins, C. Kinane and P. Gutfreund, *J. Colloid Interface Sci.*, 2014, **418**, 140–146.
27 J. C. Hunter, *J. Solid State Chem.*, 1981, **39**, 142–147.
28 S. Geller, *Acta Crystallogr., Sect. B: Struct. Crystallogr. Cryst. Chem.*, 1971, **27**, 821–828.
29 S. Tominaka, H. Yoshikawa, Y. Matsushita and A. K. Cheetham, *Mater. Horiz.*, 2014, **1**, 106–110.
30 D. M. Robinson, Y. B. Go, M. Mui, G. Gardner, Z. Zhang, D. Mastrogiovanni, E. Garfunkel, J. Li,

M. Greenblatt and G. C. Dismukes, *J. Am. Chem. Soc.*, 2013, **135**, 3494–3501.
31 F. Li, G. Parteder, F. Allegretti, C. Franchini, R. Podloucky, S. Surnev and F. P. Netzer, *J. Phys.: Condens. Matter*, 2009, **21**, 134008.
32 S. Tanuma, C. J. Powell and D. R. Penn, *Surf. Interface Anal.*, 1991, **17**, 911–926.
33 M. A. Stranick, *Surf. Sci. Spectra*, 1999, **6**, 39.
34 J. Zhang, *PEM fuel cell electrocatalysts and catalyst layers: Fundamentals and applications*, Springer-Verlag, London, 2008.